

# Experimental study of $\eta$ meson photoproduction reaction at MAMI

V. L. Kashevarov<sup>1,2,a</sup> for A2 Collaboration at MAMI

<sup>1</sup>*Institut für Kernphysik, Johannes Gutenberg-Universität Mainz, D-55099 Mainz, Germany*

<sup>2</sup>*Lebedev Physical Institute, 119991 Moscow, Russia*

**Abstract.** New data for the differential cross sections, polarization observables  $T$ ,  $F$ , and  $E$  in the reaction of  $\eta$  photoproduction on proton from the threshold up to a center-of-mass energy of  $W=1.9$  GeV are presented. The data were obtained with the Crystal-Ball/TAPS detector setup at the Glasgow tagged photon facility of the Mainz Microtron MAMI. The polarization measurements were made using a frozen-spin butanol target and circularly polarized photon beam. The results are compared to existing experimental data and different PWA predictions. The data solve a long-standing problem related the angular dependence of older  $T$  data close to threshold. The unexpected relative phase motion between  $s$ - and  $d$ -wave amplitudes required by the old data is not confirmed. At higher energies, all model predictions fail to reproduce the new polarization data indicating a significant impact on our understanding of the underlying dynamics of  $\eta$  meson photoproduction. Furthermore, we present a fit of the new data and existing data from GRAAL for  $\Sigma$  asymmetry based on an expansion in terms of associated Legendre polynomials. A Legendre decomposition shows the sensitivity to small partial-wave contributions. The sensitivity of the Legendre coefficients to the nucleon resonance parameters is shown using the  $\eta$ MAID isobar model.

## 1 Introduction

The most baryon spectroscopy data have been obtained using  $\pi N$  scattering data. Pion photoproduction on nucleons is some additional tool for the investigation of the nucleon resonances, especially in case of small  $\pi N$  partial width. Compared to pion,  $\eta$  photoproduction has some additional advantages. First, the  $\eta NN$  coupling is very small. For example, this value of  $g_{\eta NN}^2/4\pi = 0.4 \pm 0.2$  was obtained in Ref. [1] in an analysis of the angular distributions of  $\eta$  photoproduction, that is by  $\sim 30$  times smaller than for pions. Second, because of the isoscalar nature of the  $\eta$  meson, only nucleon excitations with isospin  $I = 1/2$  contribute to the  $\gamma N \rightarrow \eta N$  reactions. Both these factors simplify the extraction of the nucleon resonance parameters.

The special feature of the  $\gamma N \rightarrow \eta N$  reaction is the dominance of the  $E_{0+}$  multipole amplitude, which is populated by the  $N^*(1535)1/2^-$  and  $N^*(1650)1/2^-$  resonances. An interference between these resonances successfully explained a narrow structure in the total cross section of  $\eta$  photoproduction off the neutron [2]. Experimental data for the total cross section of the  $\gamma p \rightarrow \eta p$  reaction together with two PWA predictions are shown in Fig. 1. Partial resonance and non-resonance contributions to the total cross sections are shown in Fig. 2 as an example of the  $\eta$ MAID predictions [5],[6]. The dominant role of the  $N^*(1535)1/2^-$  is illustrated in the left panel of the Fig. 2. Despite the fact that the Born terms give an insignificant contribution, a visible non-resonance background remains

due to  $\rho$  and  $\omega$  exchange in the  $t$ -channel (black and green lines in the left panel for two version of the  $\eta$ MAID predictions). Other possible resonance contributions lie below the background (right panel). Nevertheless these resonances can be identified by using the interference with the dominant  $E_{0+}$  multipole amplitude in the polarization observables.

In this paper, new experimental data for the  $\gamma p \rightarrow \eta p$  reaction will be presented together with preliminary results of the partial-wave analysis based on the Legendre fit to the data and the  $\eta$ MAID isobar model.

## 2 Experimental setup and data analysis

The experiment was performed at the MAMI C accelerator in Mainz [7] using the Glasgow-Mainz tagged photon facility [8]. The quasi-monochromatic photon beam covered the energy range from 700 to 1450 MeV. The experimental setup is shown schematically in Fig. 3. The bremsstrahlung photons, produced by the electrons in a  $10 \mu\text{m}$  copper radiator and collimated by a lead collimator, impinged on a target located in the center of the Crystal Ball detector [9]. This detector consists of 672 optically isolated NaI(Tl) crystals with a thickness of 15.7 radiation lengths covering 93% of the full solid angle. For charged-particle identification a barrel of 24 scintillation counters (Particle Identification Detector [10]) surrounding the target was used. The forward angular range  $\theta = 1 - 20^\circ$  is covered by the TAPS calorimeter [11]. TAPS consists of 384 hexagonally shaped BaF2 detectors, each of which

<sup>a</sup>e-mail: kashev@kph.uni-mainz.de

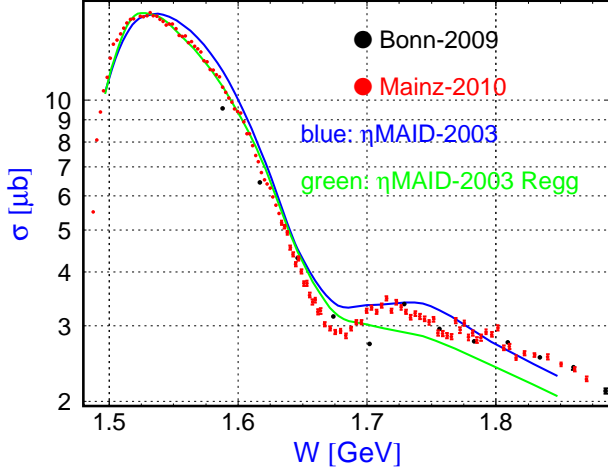


**Figure 1.** Total cross section of the  $\gamma p \rightarrow \eta p$  reaction. Black circles: Bonn data [3], red circles: Mainz data [4], blue curve:  $\eta$ MAID isobar model [5], green curve: reggeized  $\eta$ MAID isobar model [6].

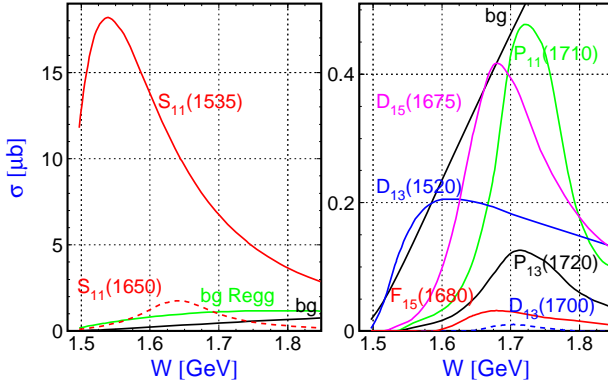


**Figure 2.** Partial contributions to the total cross sections from different resonances, predicted by  $\eta$ MAID isobar model [5] and non-resonance background for two  $\eta$ MAID versions: bg [5] and bgRegg [6].

is 25 cm long, which corresponds to 12 radiation lengths. A 5-mm thick plastic scintillator in front of each module allows the identification of charged particles. The solid angle of the combined Crystal Ball and TAPS detection system is nearly 97% of  $4\pi$  sr. More details on the energy and angular resolution of the CB and TAPS detector system are given in Ref. [12].

In the polarization measurements, a longitudinally polarized electron beam with an energy of 1557 MeV and a polarization degree of 80% was used. The longitudinal polarization of electrons is transferred to circular polarization of the photons during the bremsstrahlung process in a radiator. The degree of circular polarization depends on the photon energy and ranged from 65% at 700 MeV to 78% at 1450 MeV [13].

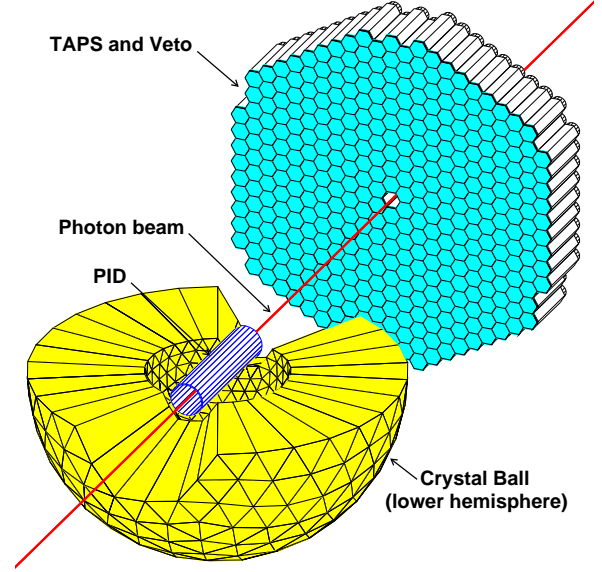


**Figure 3.** Experimental setup. The upper hemisphere of the Crystal Ball is omitted to show the inside region.

The experiment requires transversely (or longitudinally) polarized protons, which were provided by a frozen-spin butanol ( $C_4H_9OH$ ) target. A specially designed  $^3He/^4He$  dilution refrigerator was built in order to maintain a temperature of 25 mK during the measurements. The target container, length 2 cm and diameter 2 cm, was filled with 2-mm diameter butanol spheres with a packing fraction (filling factor) of around 60%. The average proton polarization was 70% with relaxation times of around 2000 h. The target polarization was measured at the beginning and the end of each data taking period. In order to reduce the systematic errors, the direction of the target polarization vector was regularly reversed during the experiment. More details about the construction and operation of the target are given in Ref. [14].

The mesons were identified via the  $\eta \rightarrow 2\gamma$  or  $\eta \rightarrow 3\pi^0 \rightarrow 6\gamma$  decays. Selections on the  $2\gamma$ , or  $6\gamma$ , invariant mass distributions and on the missing mass  $MM(\gamma p, \eta)$ , calculated from the initial state and the reconstructed  $\eta$  meson, allowed for a clean identification of the reaction. In order to subtract a background coming from quasi-free reactions on  $^{12}C$  and  $^{16}O$  nuclei of the butanol target, measurements on a pure carbon and a liquid hydrogen target were used.

### 3 Results

Figure 4 shows our preliminary results for differential cross sections together with various theoretical predictions [4, 5, 15–17] for different bins in the incoming photon energy as a function of the  $\eta$  meson polar angle in the center-of-mass system,  $\theta_\eta^*$ . The present data agree well with previous measurements, but are much more precise. The original data have a fine binning in energy, from 4 to 10 MeV, and span the full angular range. The data presented are

averages over larger energy bins to be use for Legendre fits (see below). All model predictions are in reasonable agreement with the data.

Figures 5 and 6 show our results for  $T$  and  $F$  asymmetries [18] together with previous data for  $T$  [19]. The main inconsistencies with the existing data [19] are in the near threshold region. Here, our results do not confirm the observed nodal structure in the angular dependence of the  $T$  asymmetry and solve the long-standing question related to the relative phase between  $s$ - and  $d$ -wave amplitudes. Our data do not require any additional phase shift beyond a Breit-Wigner parametrization of resonances. This important conclusion is corroborated by preliminary data from ELSA [20]. At higher energies, all existing theoretical predictions of both  $T$  and  $F$  are in poor agreement among themselves and with our experimental data, even though they describe the unpolarized differential cross sections well, see Fig. 4. The new data will therefore have a significant impact on the partial-wave structure of all models.

#### 4 Legendre analysis

The full angular coverage of our new differential cross sections and polarization observables allow us to perform a quality fit with the Legendre series truncated to a maximum orbital angular momentum  $\ell_{\max}$ :

$$\frac{d\sigma}{d\Omega} = \sum_{n=0}^{2\ell_{\max}} A_n^\sigma P_n^0(\cos \Theta_\eta), \quad (1)$$

$$T(F) \frac{d\sigma}{d\Omega} = \sum_{n=1}^{2\ell_{\max}} A_n^{T(F)} P_n^1(\cos \Theta_\eta), \quad (2)$$

$$E \frac{d\sigma}{d\Omega} = \sum_{n=0}^{2\ell_{\max}} A_n^E P_n^0(\cos \Theta_\eta), \quad (3)$$

$$\Sigma \frac{d\sigma}{d\Omega} = \sum_{n=2}^{2\ell_{\max}} A_n^\Sigma P_n^2(\cos \Theta_\eta), \quad (4)$$

where  $P_n^m(\cos \Theta_\eta)$  are associated Legendre polynomials.

The spin-dependent cross sections,  $Td\sigma/d\Omega$ ,  $Fd\sigma/d\Omega$ ,  $Ed\sigma/d\Omega$ , and  $\Sigma d\sigma/d\Omega$  were obtained by multiplying the corresponding asymmetries with our new differential cross sections. Besides the observables  $T$  and  $F$ , we used for the Legendre fit our preliminary data for the double polarization observable  $E$  (circularly polarized photon beam and longitudinally polarized target) and the photon beam asymmetry  $\Sigma$  (linearly polarized photon beam and unpolarized target) measured at the GRAAL facility [21]. Our preliminary data for the spin-dependent cross sections together with results of the Legendre fit with  $\ell_{\max} = 3$  are shown in Figs 7, 8, 9, 10.

The results for the Legendre coefficients are presented in Figs. 11 and 12 (black circles). The last coefficient,  $A_6$ , depends only on  $f$ -wave contribution,  $A_5$  is dominated by the an interference between  $d$  and  $f$  waves,  $A_4$  includes  $d$ ,  $f$  waves and an interference between  $p$  and  $f$  waves, and so on. The first coefficient,  $A_0^\sigma$ , includes all possible partial-wave amplitudes and reflects the magnitude of the

total cross section. As expected the coefficient in a good agreement with the  $\eta$ MAID prediction (red line). The coefficients  $A_n^\Sigma$  are also in reasonable agreement with the predictions, because the  $\Sigma$  asymmetry was included to the  $\eta$ MAID fit.

The fact that deviations of the  $\eta$ MAID prediction for the coefficients  $A_1^\sigma$ - $A_5^\sigma$  (top row in Fig. 11) are much larger than for the differential cross sections themselves (see Fig. 4) prompted us to involve these coefficients instead the differential cross sections in the data base for obtaining a new solution of the  $\eta$ MAID isobar model. Results of the  $\eta$ MAID fit to the coefficients  $A_0^\sigma$ - $A_6^\sigma$  (Solution 1) are shown in Fig. 11 as blue curves. Solution 1 significantly improved the description of the coefficients  $A_1^\sigma$ - $A_6^\sigma$ , but ruined all others. Results of the  $\eta$ MAID fit to the all coefficients,  $A_n^\sigma$ ,  $A_n^T$ ,  $A_n^F$ ,  $A_n^\Sigma$ , (Solution 2) are shown in Fig. 12. This very preliminary solution is much better suited to describe the entire dataset, especially for the lowest coefficients,  $A_1$ ,  $A_2$ . Probably involving additional resonances in the model will improve the situation with more high coefficients. Here we just demonstrated the impact of the new data for future partial-wave analyses. New  $\eta$ MAID predictions based on Solution 2 for the observables  $T$  and  $F$  are shown in Fig. 13 (blue lines).

#### 5 Summary

In summary, we have presented new experimental data for the target asymmetry  $T$ , the transverse beam-target observable  $F$ , preliminary data for the longitudinal beam-target observable  $E$  and the differential cross sections for the  $\gamma p \rightarrow \eta p$  reaction. All existing solutions from various partial-wave analyses fail to reproduce the new polarization data. A Legendre decomposition of the new results shows the sensitivity to small partial-wave contributions. We presented also results of the fit to the new data with the Legendre series truncated to a maximum orbital angular momentum  $\ell_{\max}$ . Preliminary  $\eta$ MAID fit to the obtained Legendre coefficients results a new solution which much better describes the new polarization data. Further improvement could be due to the addition of new resonances in the model, involving others polarization observables, extending energy region for the data.

#### Acknowledgment

This work was supported by the Deutsche Forschungsgemeinschaft (SFB 1044).

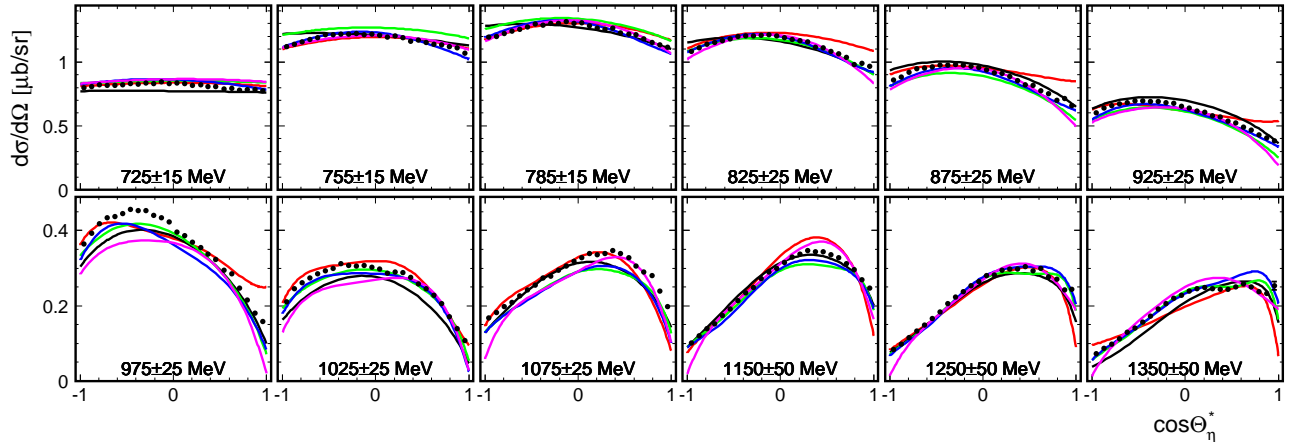


**Figure 4.** Differential cross sections. The new preliminary data with statistical uncertainties (black circles) are compared to existing partial-wave analysis predictions (red lines:  $\eta$ -MAID [5], blue: SAID GE09 [4]), green: BG2011-02 [15], black: Giessen model [16], magenta: Tryasuchev model [17]. The energy labels on the bottom of each panel indicate the photon energy bins for our data.

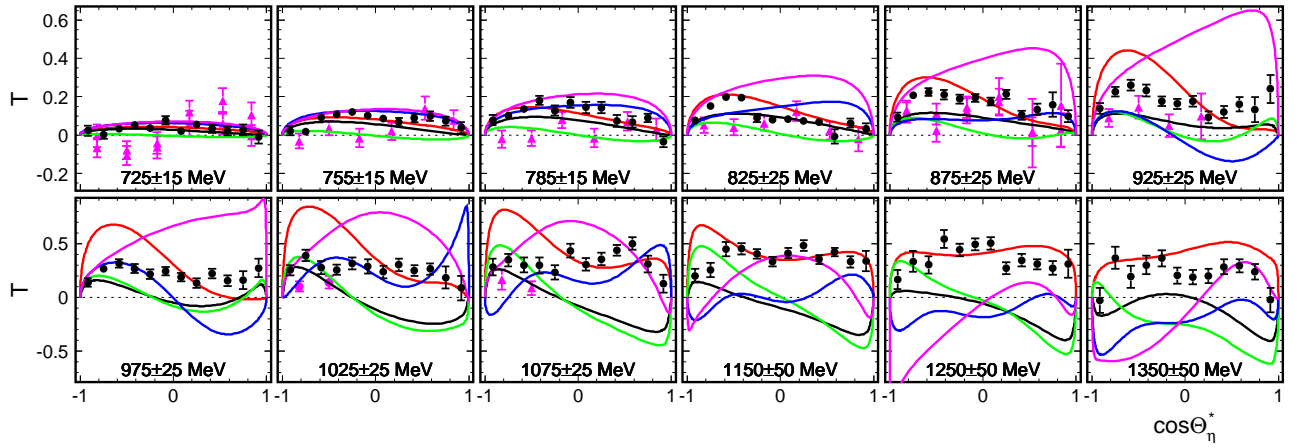


**Figure 5.**  $T$  asymmetry. The new Mainz results [18] (black circles) are compared to existing data from Bonn [19] (magenta triangles). Other notations same as in Fig. 4.

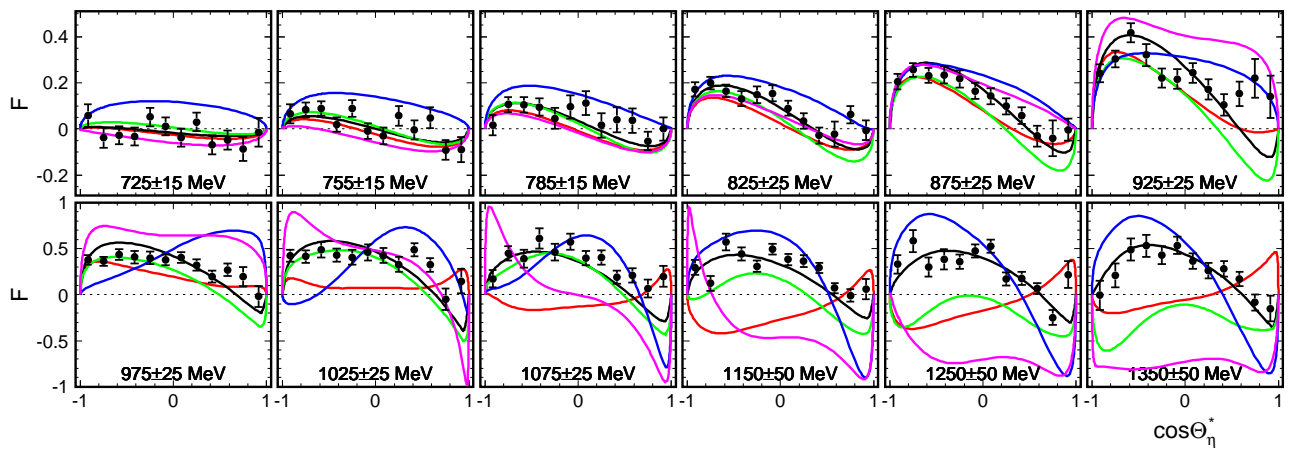


**Figure 6.** The new Mainz results [18] for  $F$  asymmetry. Notations same as in Fig. 4.

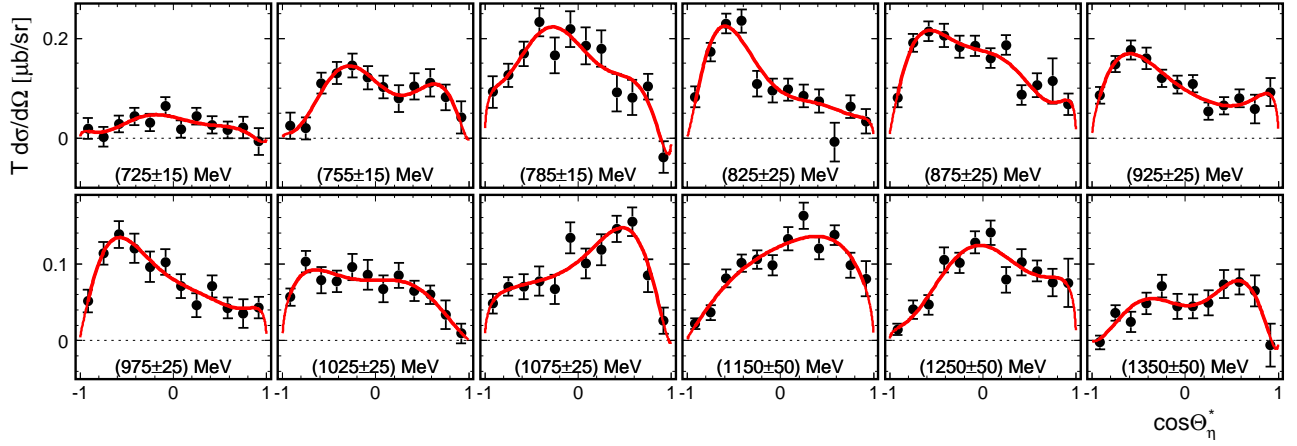


**Figure 7.** Our preliminary data for  $T d\sigma/d\Omega$ . The result of the Legendre fit with  $\ell_{\max} = 3$  is shown by the red curves.

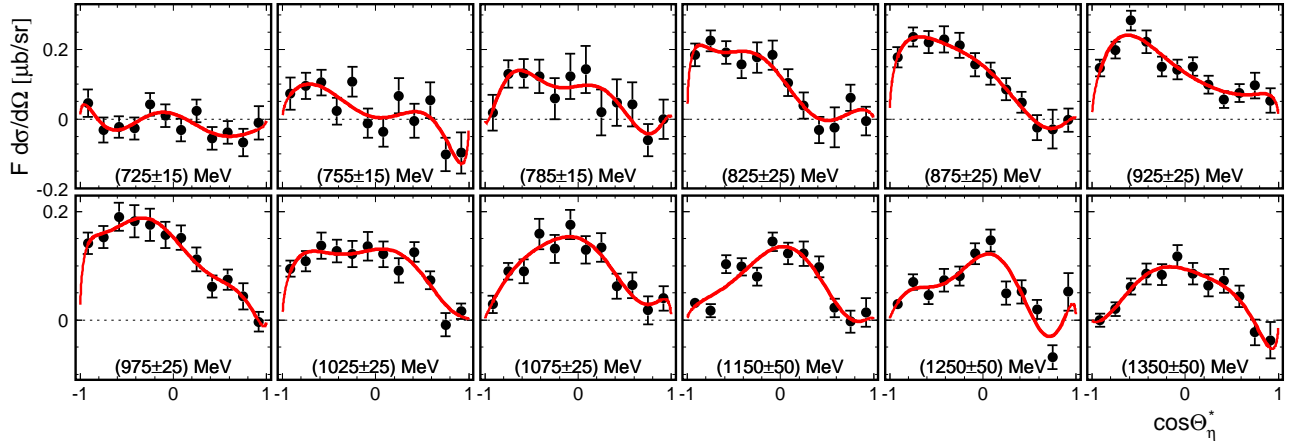


**Figure 8.** The same as Fig. 7 for  $F d\sigma/d\Omega$ .

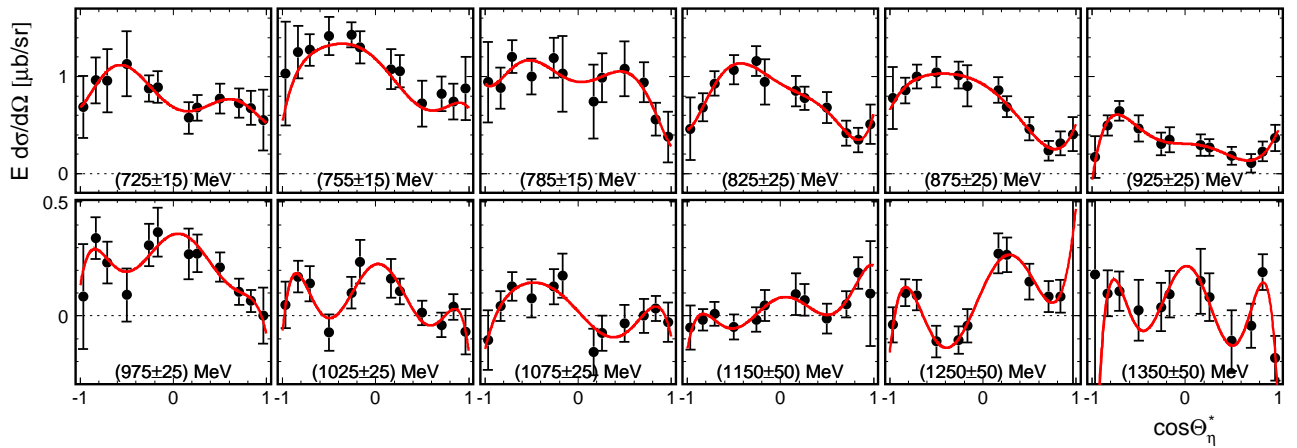


**Figure 9.** The same as Fig. 7 for  $E d\sigma/d\Omega$ .

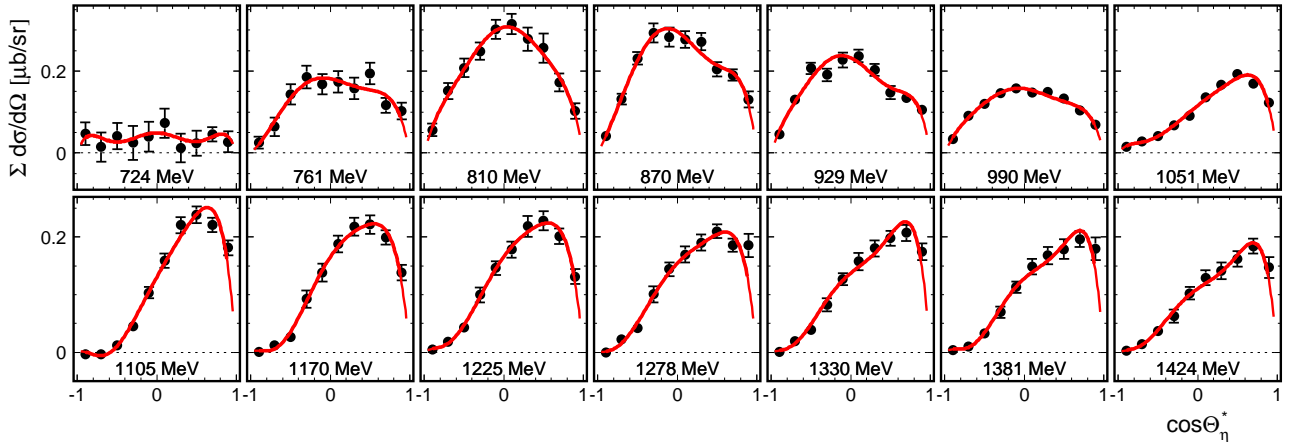


**Figure 10.**  $\Sigma$  asymmetry [21] multiplied by our new preliminary differential cross sections. Red lines are the Legendre fit result with  $\ell_{\max} = 3$ .

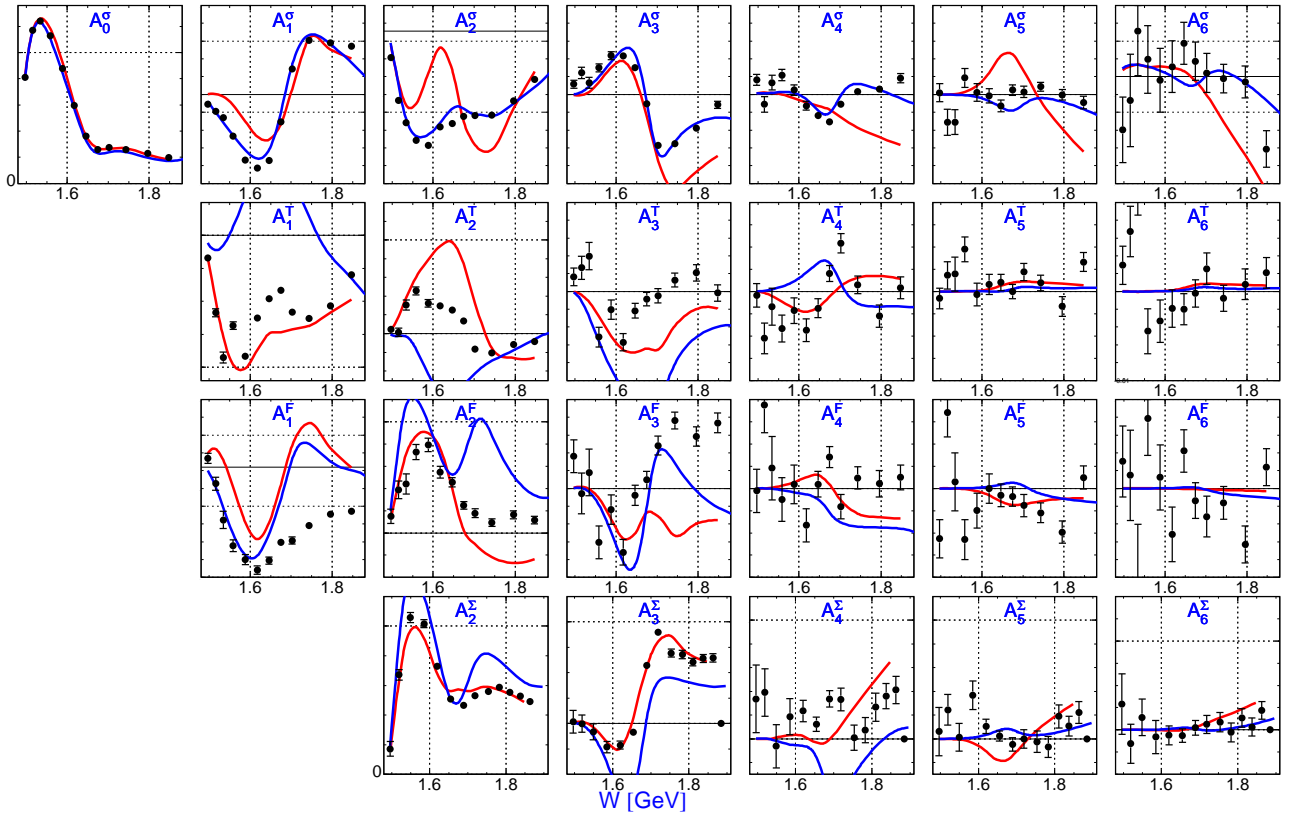


**Figure 11.** Legendre coefficients up to  $\ell_{\max} = 3$  from our fits to the different observables as function of the center-of-mass energy  $W$  (black circles). Red lines are the  $\eta$ MAID predictions. Blue lines are Solution 1.

## References

- [1] L. Tiator, C. Bennhold, S. S. Kamalov, Nucl. Phys. A **580**, 455 (1994).
- [2] A. V. Anisovich, E. Klempt, V. A. Nikonov, A. V. Sarantsev, and U. Thoma, arXiv:1402.7164.
- [3] V. Crede *et al.*, Phys. Rev. C **80**, 055202 (2009).
- [4] E. F. McNicoll *et al.*, Phys. Rev. C **82**, 035208 (2010).
- [5] W.-T. Chiang, S. N. Yang, L. Tiator, and D. Drechsel, Nucl. Phys. A **700**, 429 (2002).
- [6] W.-T. Chiang, S. N. Yang, L. Tiator, M. Vanderhaeghen, and D. Drechsel, Phys. Rev. C **68**, 045202 (2003).
- [7] K.-H. Kaiser *et al.*, Nucl. Instrum. Methods Phys. Res., Sect. A **593**, 159 (2008).

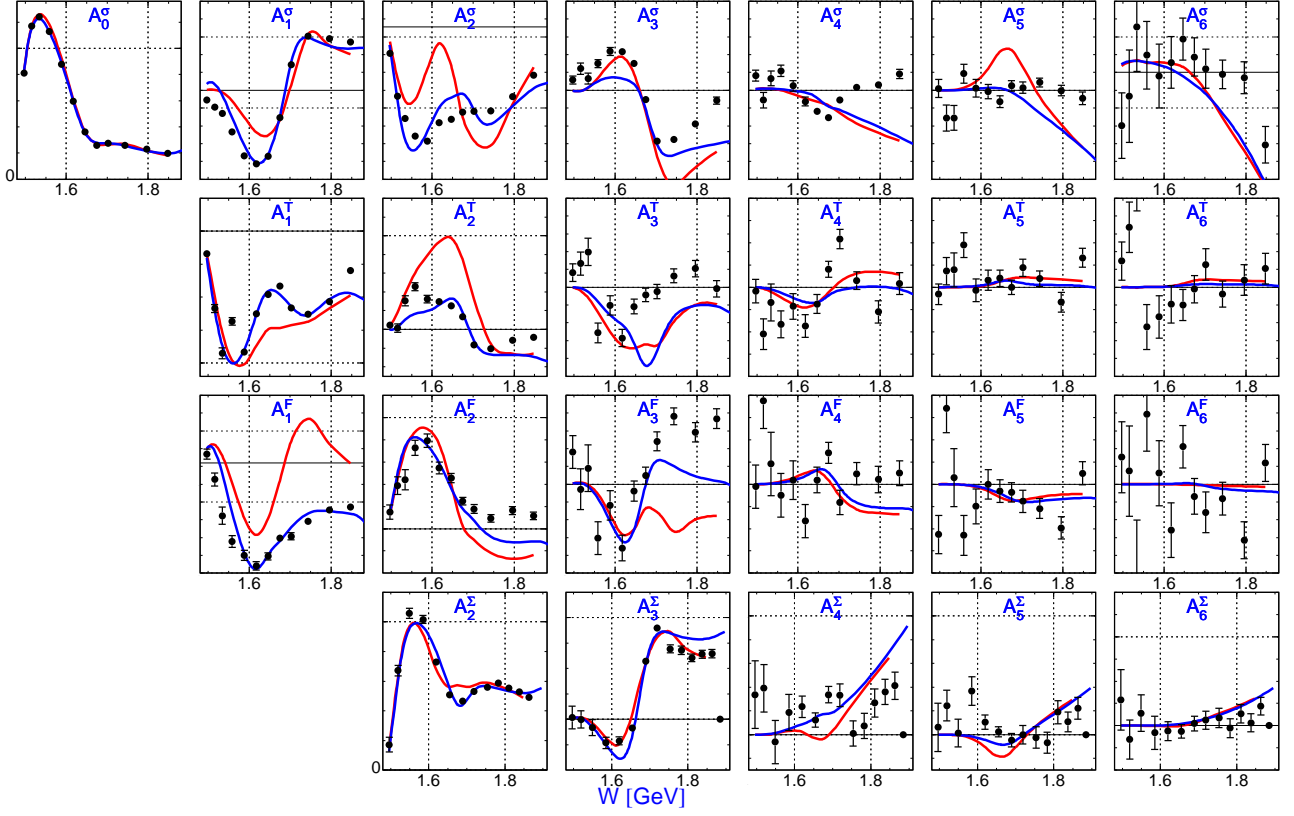


**Figure 12.** The same as Fig. 11, but blue lines are Solution 2.

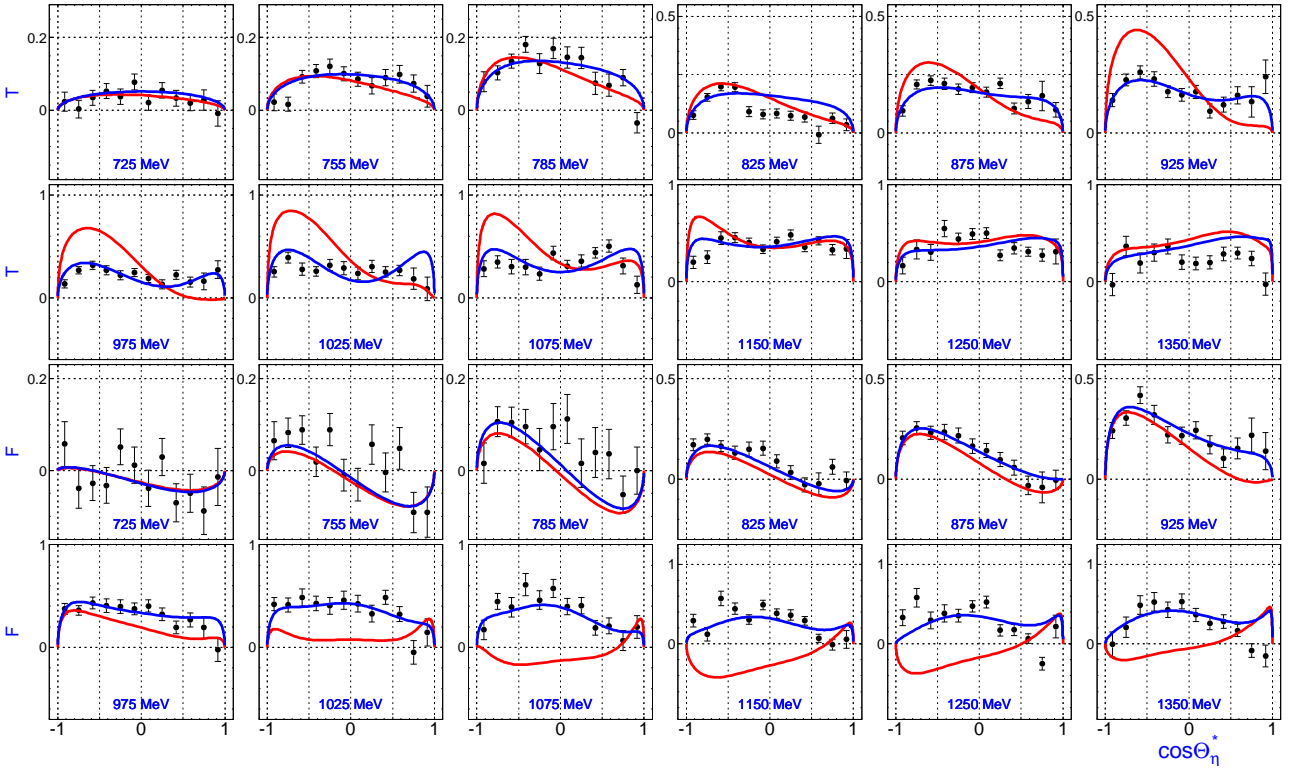


**Figure 13.** T and F asymmetries. Black circles: Mainz data [18]. Red lines:  $\eta$ /MAID prediction [5]. Blue lines: Solution 2.

- [8] J. C. McGeorge *et al.*, Eur. Phys. J. A **37**, 129 (2008); I. Anthony, J. D. Kellie, S. J. Hall, G. J. Miller, and J. Ahrens, Nucl. Inst. Instrum. Methods Phys. Res., Sect. A **301**, 230 (1991); S. J. Hall, G. J. Miller, R. Beck, and P. Jennewein, Nucl. Inst. Instrum. Methods Phys. Res., Sect. A **368**, 698 (1996).
- [9] A. Starostin *et al.*, Phys. Rev. C **64**, 055205 (2001).
- [10] D. Watts, Proc. of the 11th International Conference on Calorimetry in Particle Physics, Perugia, Italy, 2004, World Scientific, 2005, p.560.
- [11] R. Novotny, IEEE Trans. Nucl. Sci. **38**, 379 (1991); A. R. Gabler *et al.*, Nucl. Inst. Instrum. Methods Phys. Res., Sect. A **346**, 168 (1994).
- [12] S. Prakhov *et al.*, Phys. Rev. C **79**, 035204 (2009); V. L. Kashevarov *et al.*, Eur. Phys. J. A **42**, 141 (2009).
- [13] H. Olsen and L. C. Maximon, Phys. Rev. **114**, 887 (1959).
- [14] A. Thomas, Eur. Phys. J. Special Topics **198**, 171 (2011).
- [15] A. V. Anisovich, E. Klempt, V. A. Nikonov, A. V. Sarantsev, and U. Thoma, Eur. Phys. J. A **47**, 153 (2011); A. V. Anisovich, R. Beck, E. Klempt, V. A. Nikonov, A. V. Sarantsev, and U. Thoma, Eur. Phys. J. A **48**, 15 (2012).
- [16] V. Shklyar, H. Lenske, and U. Mosel, Phys. Rev. C **87**, 015201 (2013).
- [17] V. A. Tryasuchev, Eur. Phys. J. A **50**, 120 (2014).
- [18] J. Akondi *et al.*, Phys. Rev. Lett. **113**, 102001 (2014).
- [19] A. Bock *et al.*, Phys. Rev. Lett. **81**, 534 (1998).
- [20] J. Hartmann, Proc. Sci. Hadron2013 (2013) 114.
- [21] J. Ajaka *et al.*, Phys. Rev. Lett. **81**, 1797 (1998).